Title

Time-lapse 3-D electrical resistance tomography inversion for crosswell monitoring of dissolved and supercritical CO2 flow at two field sites: Escatawpa and Cranfield, Mississippi, USA

Authors
Commer, Michael
Doetsch, Joseph
Dafflon, Baptiste
et al.

Publication Date
2016-06-01

DOI
10.1016/j.ijggc.2016.03.020

Title:

Time-lapse 3-D electrical resistance tomography inversion for crosswell monitoring of dissolved and supercritical CO2 flow at two field sites: Escatawpa and Cranfield, Mississippi, USA

Authors:

Michael Commer[1], Joseph Doetsch[2], Baptiste Dafflon[1], Yuxin Wu[1], Thomas M. Daley[1], Susan S. Hubbard[1]

1: Earth Sciences - ESGG, Lawrence Berkeley National Laboratory, Berkeley, California, USA

2: SCCER-SoE, Department of Earth Sciences, ETH Zürich, Zürich, Switzerland

Corresponding author: Michael Commer

Lawrence Berkeley National Laboratory, Earth and Environmental Sciences Area

1 Cyclotron Road, Mailstop 74R316C

Berkeley, CA 94720, USA

Email-address: MCommer@lbl.gov, Telephone: (US) 510 486 6164, Fax: (US) 510 486 5686

Abstract

In this study, we advance the understanding of three-dimensional (3-D) electrical resistivity tomography (ERT) for monitoring long-term CO_2 storage by analyzing two previously published field time-lapse data sets. We address two important aspects of ERT inversion - the issue of resolution decay, a general impediment to the ERT method, and the issue of potentially misleading imaging artifacts due to 2-D model assumptions. The first study analyzes data from a shallow dissolved CO_2 injection experiment near Escatawpa (Mississippi), where ERT data were collected in a 3-D crosswell configuration. We apply a focusing approach designed for crosswell configurations to counteract resolution loss in the inter-wellbore area, with synthetic studies demonstrating its effectiveness. The 3-D field data analysis reveals an initially southwards-trending flow path development and a dispersing plume development in the downgradient inter-well region. The second data set was collected during a deep (over 3 km) injection of supercritical CO_2 near Cranfield (Mississippi). Comparative 2-D and 3-D inversions reveal the projection of off-planar anomalies onto the cross-section, a typical artifact introduced by 2-D model assumptions. Conforming 3-D images from two different algorithms support earlier hydrological investigations, indicating a conduit system where flow velocity variations lead to a circumvention of a close observation well and an onset of increased CO_2 saturation downgradient from this well. We relate lateral permeability variations indicated by an independently obtained hydrological analysis to this consistently observed pattern in the CO_2 plume's spatial evolution.

Keywords:

Geologic CO2 storage, Electrical resistivity tomography (ERT), 3-D inversion

1. Introduction

Investigations are ongoing to evaluate the feasibility of geologic sequestration of carbon dioxide (CO_2) to mitigate climatic effects due to its accumulation in the atmosphere. Suitable storage sites need to be sufficiently deep and geologically sealed in order to protect shallow freshwater aquifers and to provide conditions that maximize sequestered volumes (Hepple and Benson, 2005). After injection begins, monitoring is required to track the distribution of CO_2 and its associated reactions (Jenkins et al., 2015).

Geophysical approaches hold potential for providing information about the effectiveness of CO_2 sequestration remotely and over large volumes. Given the depth of suitable reservoirs considered for CO_2 injection, typically 800 m or deeper, crosswell geophysical approaches have resolution advantages over surface-based modes. Time-lapse crosswell seismic tomographic approaches have been used to monitor CO_2 injection experiments (e.g., Wang et al., 1998; Daley et al., 2008; Spetzler et al., 2008; Zhang et al., 2012; Ajo-Franklin et al., 2013). Other common methods are electrical resistivity tomography (ERT) (e.g., Strazisar et al., 2009; Lamert et al., 2012; Carrigan et al., 2013; Schmidt-Hattenberger et al., 2013; Doetsch et al., 2013; Auken et al., 2014; Yang et al., 2015), and low-frequency crosswell electromagnetics (e.g., Wilt et al., 1995; Hoversten et al., 2002; Girard et al., 2011). Among these techniques, electrical resistivity measurements are economically attractive and amenable to remote and autonomous data acquisition and processing. Electrical methods complement seismic methods due to their sensitivity to fluid properties, such as water saturation, phase change, ion concentration, pH, and induced geochemical changes, thus covering a large range of CO_2-induced state changes.

Cost-effectiveness is likely to remain a crucial factor for the management of future experimental and industrial CO_2 sequestration sites. Owing to drilling costs, limitations on the number of monitoring wells and their resultant adverse effects on data acquisition and resolution can thus be expected for candidate CO_2 repositories without previous oil and gas production history. The main purpose of this work is hence to shed more light on the capability of tracking CO_2-induced subsurface changes in a 3-D and time-lapse manner using the ERT technique. Specifically, two important aspects of ERT are addressed. These are resolution issues due to a disadvantageous ratio between vertical extent and interwell distances, and secondly, potential artifacts in multi-dimensional inversion outcomes.

For the first focus area, resolution issues, we investigate a case where, despite the presence of an array of four monitoring wells, central target resolution remains weak due to a large well separation relative to the actual vertical reservoir extent. This kind of problem is common in monitoring scenarios where one wants to maximize the investigation volume with a limited number of wells. One result of this issue is that reconstructed resistivity magnitudes of the inter-well region are underestimated (Ramirez et al., 2003; Kiessling et al, 2010). To alleviate this problem, we use a focusing 3D inversion approach, and demonstrate via synthetic studies and field data inversion that the resolution issue can be mitigated. Given some prior knowledge about a target zone's location and extent, focusing inversion essentially tries to counteract the quickly decaying model resolution with depth/distance. Different approaches have been developed, such as depth-weighted regularization (Li and Oldenburg, 1998) and re-weighted conjugate gradient methods with focusing stabilizers (Zhdanov 2002). The technique utilized here involves the application of a simple geometrical weighting function (Commer et al., 2011), applied here specifically for the given crosswell setting. The function is applied to the gradient vector of a non-linear conjugate-gradient (NLCG) inverse optimization scheme. The method is implemented in a NLCG imaging software package that will be referred to as EMGeo throughout this article for brevity (Commer et al., 2011).

The second focus area of this article, inversion artifacts, is motivated by earlier comparative studies on

2-D versus 3-D inversion of data containing actual 3-D signatures. These studies have raised the concern that the restriction to two model dimensions, by not honoring a target's actual inherent three-dimensionality, lets 2-D images suffer from artifacts (Papadopoulos et al., 2007; Nimmer et al., 2008; Hübert, 2012; Feng et al., 2014). This concern applies when imaging resistivity anomalies due to a CO_2 plume migrating through complex reservoir geology. A second field data set is analyzed with regard to this concern and provides a time-lapse sequence of CO_2 plume development in a deep reservoir. While the investigated volume is limited by a two-well setup, sensitivity studies indicate a certain lateral resolution perpendicular to the well plane. In order to identify potential artifacts due to 2-D model assumptions, we carry out comparative 2-D versus 3-D inversions. Subsequent comparative 3-D inversions with two different algorithms show consistent time-lapse resistivity anomalies. For further indicators of their consistency, we draw on the potential of hydrological inversion results for supplying complementary information that aids a more comprehensive ERT data interpretation (e.g. Koch, 2009; Kowalsky et al., 2011).

2. Field data inversion 1: Shallow CO_2 injection experiment at Escatawpa

Crosswell ERT data was acquired at the Victor J. Daniel Electric Generating Plant, near Escatawpa, Mississippi, USA, with the major objective of investigating the in situ effect of dissolved CO_2 on groundwater quality. Trautz et al. (2013) provide a description of the shallow injection experiment, with its well layout sketched in Figure 1. Dissolved CO_2 was delivered into a shallow aquifer through the eastern injection well. The geology can be sectioned into four major units. According to Trautz et al. (2013), the upper 30.5 m consist of sand and gravel, which is further underlain by low-permeability clay down to a depth of 46.9 m. The actual injection zone is composed of silty fine sand with minor clay; its upper boundary is at 46.9 m and its lower boundary at 54.6 m is interpreted to as the top of a thick clay package. All the wells are fully cased except within the confined aquifer depth interval which was screened. The water level in the wells was about 10 m below the ground surface. Injection took place between October 18th, 2011 and March 23rd, 2012.

ERT measurements were carried out to aid the detection of geochemical alterations in shallow groundwater due to dissolution. The pH decrease caused by dissolved CO_2 facilitates mobilization of ions and trace metals (Zheng et al., 2009). Concurrent with higher ion content is the decrease in electrical resistivity. Dafflon et al. (2013) interpreted electrical resistivity and phase responses along 2-D planes as a function of dissolved CO_2 injection processes. Specifically, they interpreted resistivity to initially decrease due to increase of bicarbonate and dissolved species. While pH stayed low until the end of the injection experiment, the resistivity rebounded earlier toward initial conditions because of the decreasing total concentration of dissolved species (and thus water conductivity). This likely occurred because of the quick depletion of some metals and fast-dissolving carbonates from the sediments due to the continuous mobilization at the plume front. Relevant for our studies is the effect of these geochemical alterations on the groundwater electrical conductivity, namely increased conductivity (decreased resistivity) due to higher ion content.

2.1. ERT survey design at the Escatawpa site

A pressure gradient was established by means of one pumping well in the northwestern quadrant (Figure 1a). Crosswell seismic, gamma logging, and ERT were performed using an array of four monitoring wells. A string of 14 ERT electrodes with a vertical electrode spacing of 0.35 m was placed in each of the four monitoring wells named MW-1, MW-2, MW-3 and MW-4. The four screened intervals span a range from 46.9 to 54.6 m below ground surface. The electrode arrays were employed as a borehole cable hanging inside each 4.57 m screened interval section, with an exact array length of

4.55 m. This electrode layout had the purpose of illuminating the inner zone between the monitoring wells which was identified as the plume's main pathway during the initial injection phase. Dipole-dipole electrode configurations were employed between each pair of wellbores. Each inverted data set involves 132 source current electrode pairs and a total of 1070 voltage data points over the whole receiver electrode array. Dafflon et al. (2013) provide additional details about the ERT field experiment and concurring laboratory column experiments.

2.2. Sensitivity study and synthetic data inversion

Figure 1 further highlights the relatively large aspect ratio between well separation and the total screened interval of the borehole, compromising the sensitivity for the target region. The average ratio *well-separation*/*screen-length* for this survey layout amounts to 2.6, whereas LaBrecque et al. (1996) recommend a range of 0.5 to 0.75 for optimal image resolution. Preceding the field data inversion, we therefor perform a synthetic inversion study with a twofold purpose. First, we investigate to what degree a conductive plume in the central region between the wells can be delineated. Second, we demonstrate how the low sensitivity in the target zone can be counteracted by a focusing inversion technique. We employ a finite-difference inverse modeling algorithm that was developed for controlled-source EM data (Newman and Alumbaugh, 2000). The inversion driver uses an iterative NLCG optimization scheme chosen for its minimal memory storage requirements (Commer et al., 2011).

In order to illuminate the inter-well region, we predefine a weighting function that is applied to the gradient vector of the NLCG inverse scheme. This concept is related to re-weighted conjugate gradient methods (Zhdanov, 2002). In our application, we counteract the highly contrasting model resolution between the borehole and inter-well region by assigning weighting coefficients to the gradient vector from which the NLCG scheme computes the model update in the model search space. See also Commer et al. (2011) for an application of this method to surface DC data. Each gradient vector component is assigned to one cell parameter of the 3-D inversion domain. The weighting coefficients are based on the inverse of the distance between the cell parameter and the nearest well. The gradient weighting function's focusing effect is thus achieved by damping the magnitude of model updates belonging to the most sensitive cell parameters near wells, while parameters from remote cells, i.e. those with low sensitivities, remain unaltered. Figure 2 illustrates this spatial behavior of the weighting function. Weighting coefficients assume values between 0 (completely damped) and 1 (no effect). Damped model regions, where weighting factors assume values below 1, appear as concentric (blue) circles around the wells.

To demonstrate the benefit of the focusing inversion, two synthetic inversions are carried out, where the synthetic data employs the same ERT configuration as the actual field observations. The target to be resolved is a 10 Ωm plume with ellipsoidal shape, located in the inter-well region, and embedded within a 47.6 Ωm resistive half space (Figure 3a). We use the same half-space value that will be chosen in the actual field data inversions below. The first inversion does not employ the gradient weighting technique (Figure 3b). While a central resistive zone can be identified, its resistivity remains underestimated. Minimal resistivity values amount to approximately 26 Ωm. Use of the weighted gradients leads to a better delineation of the resistive anomaly structure and a better estimate of its actual resistivity (Figure 3c). Here, the central region's true resistivity minimum of 10 Ωm is reproduced. Obtaining accurate resistivity is of course crucial to quantitative interpretation of CO_2 impacts.

In both images, one notes the occurrence of imaging artifacts in the form of resistivity overshoots above and below the screen intervals. Imaging artifacts in regions of insufficient model resolution are inherent to underdetermined ERT inverse problems (Carrigan et al., 2013; Friedel, 2003). This issue needs to be addressed by adequate preceding sensitivity studies in order to avoid biased interpretations of insufficiently resolved model regions. For this purpose, we analyze the sensitivity decay with distance by means of a sensitivity map. Model cell parameter sensitivities are quantified in Figure 4a for a horizontal slice through the common center of the screened depths (z=49.75 m), and in Figure 4b for a vertical slice through the central target region (y=299 m). Electrode positions are projected onto the sections. The individual sensitivity for a given cell parameter, m, is calculated by means of a model perturbation by the quantity $\Delta\sigma_m$, chosen to be 10 % of the true plume model (Figure 3a),

$$S_m = \log_{10}\left(\frac{\sum_{i=1}^{N}\left|d_i^0 - d_i^m\right|}{\Delta\sigma_m}\right). \qquad (1)$$

The term involves the cumulative absolute data differences between the responses d_i^0 and d_i^m of the unperturbed model and perturbed model, respectively, where N denotes the total number of data points. For an understanding of how this measure relates to the actual data perturbation, it is useful to determine the largest individual relative change of a single data point i, $\frac{\left|d_i^0 - d_i^m\right|}{\left|d_i^0\right|}\times 100$ (in %), which in this case amounts to 19.7 %. The sensitivities of Equation 1 are further normalized by the global maximum of S_m, i.e. the plotted quantities are $S_m^{norm} = \frac{S_m}{\max(S)}$. The sensitivity maps of Figure 4 confirm the common observation in borehole ERT - objects close to boreholes are well resolved, while objects in the middle between boreholes are poorly resolved (Day-Lewis et al., 2005).

2.3. Time-lapse 3-D field data inversions

We have carried out 3-D inversions for 11 data sets spanning 131 days after injection at the Escatawpa site,, analyzing all six transects between the four wells. To obtain time-lapse images of the electrical resistivity change, we employ a ratio-type inversion method. This method uses normalization with a baseline data set to produce comparative images rather than images of absolute electrical resistivity (Daily and Owen, 1991). Thus, the input to our imaging tool consists of electrical field ratios $E(t)/E_0$ at time t, where E_0 is the baseline data at (pre-injection) time t=0. The ratio inversion method has been shown to be beneficial for the removal of modeling errors and systematic measurement errors (Doetsch et al., 2013). Table 1 summarizes the number of inverted ERT source-receiver configurations. To counteract weak resolution in the inter-well region, the focusing method was employed using the same gradient weighting function (illustrated in Figure 2) as the preceding synthetic study. A half space model with 47.6 Ωm resistivity was estimated through forward modeling trials and served as the starting model for each 3-D inversion.

Figures 5a and 5b summarize the spatial resistivity deviations, $\Delta\rho$ in percent, with respect to the pre-injection state. Each plot row marks a certain day after injection began. In Figure 5a, the left, middle and right plot columns represent vertical sections parallel to the Easting coordinate and cut through the Northing coordinates moving north from MW-2 to MW-1, N=292 m, N=300 m, and N=307 m (Figure 1). In Figure 5b, the same three plot columns represent vertical sections parallel to the Northing coordinate and cut through the Easting coordinates moving downgradient from MW-3 to MW-4, E=514 m, E=507 m, and E=499 m (Figure 1).

While the generally low resolution 3D inversion results require a rather cautionary interpretation, some important larger-scale observations can be extracted from the images shown in Figures 5a and 5b. Starting with a relatively homogeneous image at day 7, significant resistivity decreases appear on day

21 after the beginning of injection. Negative resistivity changes indicate the passing of dissolved CO_2. The southern and center Easting sections (Figure 5a, left and middle plot column) indicate a southwards shift of these changes, because of an absence of corresponding change in the northern section (right column). Starting at day 31, the center section (middle column) reveals a significant negative resistivity anomaly near MW-3. Given MW-3's proximity to the injection well, such a clear onset meets our expectation.

Dafflon et al. (2013) observed from 2-D inversion studies that the drop in resistivity in the plane between MW-2 and MW-3 rebounds at MW-3, i.e. the resistivity rises back to baseline values after passing of the plume. Noting that this rebound happened over a shorter time period than the rebound at MW-2, they concluded a spreading of the plume over time due to dispersion and heterogeneity. The spreading of significant negative changes over a larger volume downgradient from MW-3 begins on day 83, which is in agreement with the onset derived from 2-D images (Dafflon et al., 2013).

Reactive transport modeling by Trautz et al. (2013) yielded two observations with relevance for a tentative plume flow path prediction. First, a low-pH breakthrough was predicted to occur first at MW-3, then, in order of arrival, at MW-2, MW-1, and MW-4, with a relatively small arrival time gap between the latter two. Second, even 120 days after injection start, the center of the predicted pH plume is closer to the southern MW-2 - MW-3 region, with the plume boundary now arriving near MW-1 and MW-4. Both these observations point to a southern preferential flow, which is indicated by the delayed appearance of lowered resistivity in the northern image section through the MW-1 plane (Figure 5a, third column).

A shift of the early onset of lowered resistivity towards the MW-2 region is also observed from the slices in the Northing plane (Figure 5b). As expected, the image closest to the injector (left plot column) shows the most changes, in contrast to a minimal activity in the western section (right column) up to day 56. An interesting observation is the period of rather benign variations around the period of day 56, as also observed from 2-D inversions, and possibly related to rebounding resistivity drops which were also measured in laboratory studies (Dafflon et al., 2013). Peaking resistivity changes become visible in the center plane (middle column) and appear to spread out further moving downgradient (right column). Geologic heterogeneities in the inter-well region are most likely the cause for both the southwards-trending plume movement as well as the spatial plume dispersion over time.

2.4. Comparative synthetic study for the evaluation of field data inversions

A second synthetic inversion study aims at improving our understanding of the significance of the resistivity variations observed from the Escatawpa field data inversions. While the first synthetic inversion for an anomaly embedded in a homogeneous background already demonstrated the benefits of the focusing technique (Figure 3), the question remains whether the technique is similarly beneficial in the presence of more complex target structures. To address this question, using the same survey geometry as given by the field data, synthetic data is now created from the final inversion outcome of day 131 (bottom panel in Figure 5 a and b). This inversion result is deemed as a good representation of a complex model, given both positive and negative resistivity anomalies. With the principal goal of directly comparing inversion results with and without the focusing technique, we omit the addition of white Gaussian noise. Further, the same number of NLCG inversion iterations (25) is enforced for each inversion run. The results of the two synthetic inversions are shown in Figure 6, together with the original model (left column). Note again that the original model, referred to as true model, is the final field data inversion result of day 131. The middle and right column show the inversion results with gradient-weighting inactive and active, respectively, for the same six cross sections that were presented in Figure 5. Major resistivity anomalies are reproduced well by the gradient-weighting technique (right column), while the actual resistivity contrasts appear slightly underestimated. On the other hand, the results without gradient-weighting lead to a rather poor agreement with the true model.

As shown in the first synthetic study (without usage of the focusing technique), the inversion can identify a centralized anomaly in a homogeneous background (Figure 3b). This capacity is lost in the presence of more complex structures as shown in Figure 6 (true model). However, the more complex anomalies can be identified through enforcement of weighted gradients.

3. Field data inversion 2: Deep CO_2 injection experiment at Cranfield

The Cranfield ERT experiment was part of a multidisciplinary project, carried out near Natchez, Mississippi, by the Southeast Carbon Sequestration Partnership (SECARB). A detailed site and project description is given by Hovorka et al. (2013) and references therein. Designed as a pilot study, a total mass of over 1 million metric tons of CO_2 were injected in super-critical state into a permeable subsurface reservoir, located at depths over 3000 m, which is part of the Lower Tuscaloosa Formation. The reservoir has an average thickness of 30 m accessed via CO_2 injection well F-1 in Figure 7a. The formation geology is characterized by a complex system of fluvial channels composed of conglomerate with a significant component of chert (fine-grained sedimentary) pebbles in the lower parts (Kordi et al., 2010). These are overlain by fine-grained sandstones with minor interbedded mudstone. Based on petrographic data, a large degree of reservoir heterogeneity is reported, owing to contrasting porosity and permeability within this channel system (Lu et al., 2013). The injected fluid contained mostly CO_2 with a low percentage (1-2 %) of methane. For the purpose of tracer studies, small amounts of a SF6 tracer were co-injected. Temperature and pressure reservoir conditions led to a supercritical state of the injected fluids.

3.1. ERT survey design at Cranfield

While the ERT method has mostly evolved from shallow environmental studies, application for deeper sequestration monitoring, as at the Ketzin pilot experiment (Kiessling et al., 2010), has new logistical challenges. At the Ketzin and Cranfield sites, ERT has proven the capability of tracking CO_2 migration over time, owing to elevated resistivity associated with increasing saturation of gas in supercritical state (Carrigan et al., 2013; Doetsch et al., 2013).

Carrigan et al. (2013) provide details about the ERT experimental design, data processing and challenging field logistics of the deep electrode deployment. Two closely spaced monitoring wells, F-2 and F-3, were used for installation of the crosshole ERT array. The distance from F-1 to F-2 is approximately 70 m, and the distance from F-2 to F-3 is about 33 m (Figure 7a). The measurements involve four-electrode configurations, with a dipole-dipole switching schedule that has the current and potential electrode pairs sampling through both F-2 and F-3. A vertical array of 14 electrodes with 4.6 m spacing and 61 m total length was centered on the injection zone in F-2. Economic reasons led to only 7 electrodes deployed along the same array length in F-3, requiring an increase in spacing to 9.14 m (30 ft). This configuration leads to a favorable ratio of *well-separation*/perforation-*length* of approximately 0.6. Preceding comparative inversion studies revealed no additional benefit from using the focusing approach, which is likely due to the better spatial coverage.

ERT monitoring started on November 25th of 2009, five days before injection began. Our inverted data spans the time period beginning at day 13 and ending at day 103 after injection start. To obtain time-lapse images of the electrical resistivity change, we again employ the ratio-type inversion method, which has the benefit of minimizing effects due to systematic errors, such as potentially inaccurate electrode spacings. Following Doetsch et al. (2013), all inversions start with a 1 Ωm homogeneous half-space model, further using homogeneous model smoothing constraints.

3.2. Supporting hydrological information

Supporting the interpretation of the 3-D time-lapse ERT inversion results, we will draw on a hydraulic permeability model obtained from recent hydrological studies. Hydrological measurements were made in both monitoring wells and included continuous gas composition sampling, where the main recorded gas phase components were CO_2, methane, and a SF6 tracer (Doughty and Freifeld, 2013). Reservoir flow simulations and concurring inverse modeling approaches involved a three-layered hydrological model as shown in Figure 7b. The inverted hydrological data included gas mole fractions measured in both monitoring wells, with three sampling depths in each well. Jointly inverted with the mole fractions were changes in electrical conductivity, $\sigma(t)/\sigma(t=0)$, calculated from the ERT measurements and averaged over each of the three main geological layers as a function of time. Thereby, ERT measurements served as hydrological proxy data with the ERT methods' benefits to volumetric coverage, thus providing stabilizing constraints to flow and transport inverse modeling (Doetsch et al., 2013; Commer et al., 2014).

The three-layered permeability parameter distribution was supported by the analysis of borehole porosity logs strongly suggesting three distinct units with median porosities of 19.6 %, 23.9 %, and 22.9 % for layers 1, 2 and 3, respectively (Figure 7b). In subsequent hydrological inverse modeling studies, the distribution of permeability parameters over each layer was further modified in order to find a compromise between the limited spatial footprint of the hydrological data and the demand to provide a sufficient degree of freedom for lateral permeability variability. This led to a 3-D model with a total of 25 zones of varying absolute hydraulic permeability distributed over the three layers (Commer et al., 2014). The relatively coarse model parameterization is further justified by the relatively large distance from the injection source, causing the measured gas compositions to represent an effective permeability averaged over the adjacent flow paths. The final hydrological model will be integrated with ERT results further below.

3.3. 3-D sensitivity study

To obtain an estimate of the 'trust-region' that will be considered for 3-D interpretation of the following ERT inversions, we analyze the sensitivity over the inversion domain. Sensitivities are calculated using a model perturbation of the final resistivity model obtained for day 53 of the 3-D time-lapse data inversions. Our reason for this choice is that the plume volume reaches peak levels at this time (shown further below). Plotted in Figure 8 is the quantity S_m of Equation 1 normalized by its global maximum. One observes the familiar sensitivity pattern, namely elevated sensitivity near the wells, which drops rapidly away from the wells. The sensitivity range in the inter-well region spans approximately two orders of magnitude. For a visualization of the same minimal level laterally away from the well plane the sensitivity map is overlain on the isosurface pertaining to cell parameters with quantities $\log_{10}(S_m^{norm}) \geq -2$. This lets us estimate the lateral extent of the trust-region to approximately ±10 m from the well plane. The sensitivity map thus indicates that a model volume of approximately ($dx \times dy \times dz$) 40 m × 20 m × 60 m is resolved by this two-well survey configuration. However, note that due to the 2-D survey geometry, 3-D inversion cannot distinguish on which side of the cross-section plane an anomaly is located.

A distinct feature of the sensitivity distribution in Figure 8 is that large values, where $\log_{10}(S_m^{norm})$ is above -0.5, occur along the whole perforated length of F-2, while such sensitivity magnitudes occur only near the central portion of the F-3 perforated zone. While geologic heterogeneity and electrode array types may play a role in sensitivity, we believe that the coarser electrode coverage in F-3 (7 electrodes versus 14 in F-2) is the main reason for the lower sensitivity magnitudes. Therefore, we point out that a careful data interpretation needs to consider the possibility of biased imaging results due to this asymmetric sensitivity distribution.

3.4. Comparative 2-D versus 3-D inversions

The following study has the purpose of examining potential image artifacts at Cranfield due to 2-D model assumptions. Given the sensitivity distribution of Figure 8, we focus on the inter-well volume pointed out previously. We employ the tool BERT, which offers both 2-D and 3-D inverse modeling and uses a finite-element forward operator (Rücker et al., 2006) and a Gauss-Newton inversion framework (Günther et al., 2006). A qualitative comparison between both image sequences in Figure 9 yields spatially conforming snapshots of the centers where the resistivity increases over time. Note that by means of the ratio-type inversion method, these results translate to relative changes (calculated in percent) with respect to the (1 Ωm) homogeneous background. Positive values imply a resistivity increase over time. Both sequences indicate the onset of enhanced resistivity associated with increasing gas saturation after day 21, with a more pronounced contrast delivered by the 2-D inversion (right panels).

A commonality in both image types is the concentration of the highest positive variations near well F-3. The most striking difference on the other hand is a larger spatial variation near F-2 in the 2-D images. The 3-D images show more homogeneous and weaker positive changes near F-2. Further, all 2-D images appear to suggest a fragmented kind of flow path distribution, whereas the maximum 3-D resistivity changes assume more of a coherent plume shape. These discrepancies comply well with the comparative studies of Yang and Lagmanson (2006), who point out that objects not intersecting the imaging plane of a 2-D inversion may be projected onto the cross section, thus adding complexity by highlighting off-plane anomalies.

We further point out that the asymmetric sensitivity distribution revealed in Figure 8 may also have a certain effect on the 2-D images that potentially differs from the 3-D analysis. Despite these differences, the vertical extent of the main flow path between the two observation wells, between approximately 3190 m and 3210 m depth, is indicated by both inversion outcomes. The comparisons indicate that the additional degree of freedom provided by the 3-D approach does not adversely affect the imaging capacity. In other words, in the presence of insufficient sensitivity, adverse effects like major differences between 2-D and 3-D images would be triggered by the larger solution non-uniqueness.

3.5. Comparative 3-D inversions

The image comparisons shown in Figure 9 indicate potential biased resistivity structures in 2-D inversions of data recorded in geology where 3-D structures prevail. However, when allowing for more degrees of freedom in 3-D inversions, another class of imaging artifacts needs to be considered, introduced by the more underdetermined nature of the 3-D inverse problem. The comparative time-lapse inversion sequence summarized in Figure 10 attempts to qualitatively assess the degree of 3-D solution non-uniqueness. We compare 3-D images generated by the imaging code BERT (shown in the left panels and identical to the 3-D results of Figure 9) against images of the code EMGeo (right panels). Both 3-D outcomes confirm the concentration of resistivity variations shifted slightly to the lower perforated section. This is also in agreement with earlier studies, suggesting that most saturation changes occur within the more permeable and more porous reservoir layers in the lower perforated interval (Carrigan et al., 2013; Doetsch et al., 2013). The onset and concentration of saturation changes (interpreted via resistivity change) near well F-3 is also consistent in both 3-D inversions. Some differences can be observed in the magnitude of these changes in the early (before day 33) and late (after day 83) stages, whereas structural patterns have a relatively high degree of similarity. There are spatially variable reservoir attributes that have strong control over permeability and porosity in this formation, e.g. compaction and quartz overgrowth (Kordi et al., 2010). Hence, locally inhomogeneous flow paths may explain the rather inhomogeneous saturation changes near the central portion of F-3. The homogeneous and high sensitivity in the central perforated zone of the F-3 well render imaging artifacts unlikely in that zone.

3.6. Integrated hydrological and geophysical interpretation

The onset of saturation changes near well F-3 revealed by the comparative 3-D analysis confirms the findings of Lu et al. (2012) of a heterogeneous flow path system. For both injected gas and tracers, they observed faster transport between F-1 and F-3 than between F-1 and F-2. The authors suggested a system of preferential flow paths that respond differently to pressure gradient changes, where the F-1 - F-3 path may not be linked to F-2. Such lateral permeability variations were also indicated by core samples, with F-3 cores showing much higher permeability over F-2 cores (Lu et al., 2013). In Figure 11, we overlay an image representative of the later observation stage (EMGeo result at day 103) with the permeability model obtained from a hydrological data inversion (Commer et al., 2014). Isosurfaces show resistivity changes exceeding 5 % (grey) and 20 % (red). Overlain is the hydrological model obtained from an inversion for 25 zones of varying absolute hydraulic permeability. To limit hydrological inverse solution non-uniqueness, symmetry considerations were used to mirror these 25 parameters from one quarter of the whole hydrological modeling domain (Figure 7b) to each of the other three quadrants.

Despite the fact that the nature of hydrological data inversion is characterized by an inevitable averaging of hydrological attributes on the inter-well scale, the permeability model reflects important findings from the core analysis. Figure 11 shows two of the (symmetric) quadrants straddling the monitoring well plane at *y*=0 m. We have three observations. First, the stark permeability contrast between Layer 1 and the two lower layers confirms the low-permeability regime of the upper reservoir (a flow boundary). Second, the vertical contrast from high (Layer 2) to low (Layer 3) permeability reported for the F-3 region (near *x*=100 m) is indicated. Third, the lateral permeability variations along the direction perpendicular to the F-2 – F-3 well plane in the lower layers suggest laterally differing flow rates. This may explain CO_2 flow circumventing the F-2 well and lead to higher saturation changes near F-3, as indicated by the coincident high resistivity (red isosurface). The integrated ERT and hydrologic inversion hence strongly confirms an efficient flow path connecting the injector to F-3, as proposed by Lu et al., 2013.

4. Conclusions

By analyzing ERT time-lapse data from two pilot injection experiments, along with select synthetic data studies, we have demonstrated important aspects of 3D ERT inversions for monitoring subsurface CO_2 migration. We affirmed that the ERT method offers a direct link to both gas dissolution and supercritical gas saturation changes at the inter-borehole scale. Challenges are given by the generally underdetermined nature of the crosswell inverse problem owing to insufficient data coverage.

For the shallow Escatawpa data set, the focusing effect achieved by weighted gradients has counteracted the resolution decay away from the ERT wells. Our first synthetic comparative study demonstrated that this method has the capability of reproducing the actual contours and magnitude of a resistivity anomaly embedded in a homogeneous background and located in the inter-well region, given the favorable conditions of a homogeneous background and a spatially large anomaly. As shown by the second synthetic study, more complex anomalies could also be reproduced to a fairly good degree.

We emphasize that careful prior sensitivity assessment remains an essential prerequisite to delineate the model boundaries wherein CO_2-related resistivity changes are of significance. With respect to earlier 2-D results, the 3-D inversions have added information about the inter-well region. At Escatawpa, we observe a southwards flow pattern with respect to the injection – pumping well line, a spatially homogeneous initial plume development near the injection well, which attains increasing heterogeneity moving downgradient over time.

The time-lapse Cranfield site data provide a good test bed for studying inversion and imaging differences due to 2-D versus 3-D model assumptions. Imaging artifacts may occur due to systematic and coherent data noise. Assuming that we minimize such noise artifacts by inverting ratio-type data, a 2-D treatment in the presence of a complex fluvial channel system may project off-plane anomalies, for example near well F-2 at Cranfield. This type of artifact (typical in crosswell data) is likely to explain the main discrepancy observed in the 2-D – 3-D comparisons, i.e. a stronger onset near F-2, while the 3-D ERT images of both employed codes and the hydrological evidence suggest an initial circumvention of F-2. Notwithstanding this explanation, the additional third degree of freedom can lead to flawed interpretation due to increased solution non-uniqueness. Here, a qualitative assessment of non-uniqueness is made by a preceding sensitivity analysis and subsequent comparative 3-D inversions. We believe that the degree of lateral resolution together with consistent comparative imaging outcomes promote a 3-D treatment despite the planar ERT survey geometry.

The 3-D resistivity patterns obtained from the two different imaging algorithms at Cranfield support the existence of a heterogeneous system of fluvial deposits. As reported in earlier petrographic studies, these deposits are characterized by predominantly horizontal flow paths in the lower perforated region with laterally differing permeabilities. The underlying spatial permeability variations indicated by earlier core samples from both observation wells are consistent with the permeability model developed from hydrological analysis, which can further be well aligned with our ERT inversion results. This situation, where the project database permits a consistent joint hydrogeophysical interpretation, affirms the value of 3-D resistivity tomography for future CO_2 storage monitoring projects.

Acknowledgements

This work was funded by the Assistant Secretary for Fossil Energy, National Energy Technology Laboratory (NETL), National Risk Assessment Program (NRAP), of the US Department of Energy under Contract No. DEAC02-05CH11231 to LBNL and in collaboration with the Electric Power Research Institute. This work was also supported by SECARB and the National Risk Assessment Partnership (NRAP) through the National Energy Technology Laboratory of the U.S. Dept. of Energy. Lawrence Berkeley National Laboratory is supported under contract DE-AC02-05CH11231. The authors would like to acknowledge the assistance of Susan Hovorka (TBEG), technical lead for the Cranfield Project. We would also like to acknowledge Denbury Resources and Charles Carrigan of Lawrence Livermore National Laboratory for use of the Cranfield data. J. Doetsch was partly funded by the Swiss Competence Center for Energy Research, Supply of Electricity (SCCER-SoE). We are grateful to two anonymous reviewers, whose suggestions greatly enhanced this work.

References

Ajo-Franklin, J.B., Peterson, J., Doetsch, J., Daley, T.M., 2013. High-resolution characterization of a CO_2 plume using crosswell seismic tomography: Cranfield, MS, USA. International Journal of Greenhouse Gas Control 18, 497–509.

Auken, E., Doetsch, J., Fiandaca, G., Christiansen, A.V., Gazoty, A., Cahill, A.G., Jakobsen, R., 2014. Imaging subsurface migration of dissolved CO_2 in a shallow aquifer using 3-D time-lapse electrical resistivity tomography. Journal of Applied Geophysics 101, 31-41.

Benson, S.M., Surles, T., 2006. Carbon dioxide capture and storage: an overview with emphasis on capture and storage in deep geological formations. The Proceedings Special Issue, Institute of Electrical and Electronics Engineers (IEEE) 94, DOI 10.1109/PROC.2006.883716.

Bergmann, P., Schmidt-Hattenberger, C., Kießling, D., Rücker, C., Labitzke, T., Henninges, J., Baumann, G., Schütt, H., 2012. Surface-downhole electrical resistivity tomography applied to monitoring of CO_2 storage at Ketzin, Germany. Geophysics 77, B253–B267.

Carrigan, C.R., Yang, X., LaBrecque, D.J., Larsen, D., Freeman,D., Ramirez, A.L., Daily, W., Aines, R., Newmark, R., Friedmann, J., Hovorka, S.D., 2013. Electrical resistance tomographic monitoring of CO_2 movement indeep geologic reservoirs. International Journal of Greenhouse Gas Control 18, 401-408.

Christensen, N.B., Sherlock, D., Dodds, K., 2006. Monitoring CO_2 injection with crosshole electrical resistivity tomography. Exploration Geophysics 37, 44–49.

Commer, M., Newman, G.A., Williams, K.H., Hubbard, S.S., 2011. Three-dimensional induced polarization data inversion for complex resistivity. Geophysics 76, F157-171, 2011.

Commer, M., Kowalsky, M.B., Doetsch, J., Newman, G.A., Finsterle, S., 2014. MPiTOUGH2: A parallel parameter estimation framework for hydrological and hydrogeophysical applications. Computers and Geosciences 65, 127-135.

Dafflon, B., Wu, Y., Hubbard, S.S., Birkholzer, J.T., Daley, T.M., Pugh, J.D., Peterson, J., Trautz, R.C., 2013. Monitoring CO_2 intrusion and associated geochemical transformations in a shallow groundwater system using complex electrical methods. Environmental Science & Technology 47, 314−321.

Daily, W., Owen, E., 1991. Cross-borehole resistivity tomography. Geophysics 56, 1228-1235.

Daley, T.M., Myer, L.R., Peterson, J.E., Majer, E.L., Hoversten, G.M., 2008. Time-lapse crosswell seismic and VSP monitoring of injected CO_2 in a brine aquifer. Environmental Geology 54, 1657–1665.

Day-Lewis, F.D., Singha, K., Binley, A.M., 2005. Applying petrophysical models to radar travel time and electrical resistivity tomograms: Resolution-dependent limitations. Journal of Geophysical Research-Solid Earth 110:10.1029/2004JB003569.

Doetsch, J., Kowalsky, M.B., Doughty, C., Finsterle, S., Ajo-Franklin, J.B., Carrigan, C.R., Yang, X, Hovorka, S.D., Daley, T.M., 2013. Constraining CO_2 simulations by coupled modeling and inversion of electrical resistance and gas composition data. International Journal of Greenhouse Gas Control 18, 510–522.

Doughty, C., Freifeld, B., 2013. Modeling CO_2 injection at Cranfield, Mississippi: Investigation of methane and temperature effects. Greenhouse Gas Sci. Technol. 3, 475–490

Feng D.S., Dai Q.W., Xiao, B., 2014. Contrast between 2D inversion and 3D inversion based on 2D high-density resistivity data, Transactions of Nonferrous Metals Society of China 24, 224-232.

Friedel, S., 2003. Resolution, stability and efficiency of resistivity tomography estimated from a generalized inverse approach. Geophysical Journal International 153, 305-316.

Girard, J.-F., Coppo, N., Rohmer, J., Bourgeois, B., Naudet, V., Schmidt-Hattenbergerber, C., 2011. Time-lapse CSEM monitoring of the Ketzin (Germany) CO2 injection using 2×MAM configuration. Energy Procedia 4, 2011, 3322–3329.

Günther, T., Rücker, C., Spitzer, K., 2006. Three-dimensional modelling and inversion of dc resistivity data incorporating topography – II. Inversion. Geophysical Journal International 166, 506–517.

Hepple, R.P., Benson, S.M., 2005. Geologic storage of carbon dioxide as a climate change mitigation strategy: performance requirements and the implications of surface seepage. Environmental Geology 47, 576-585.

Hoversten, G.M., Roland, G., Washbourne, J., Daley, T.M., 2002. Pressure and fluid saturation prediction in a multicomponent reservoir, using combined seismic and electromagnetic imaging. Geophysics 68, 1580-1591.

Hovorka, S.D., Meckel, T.A., Trevino, R.H., Lu, J., Nicot, J.-P., Choi, J.-W., Freeman, D., Cook, P., Daley, T.M., Ajo-Franklin, J.B., Freifeld, B.M., Doughty, C., Carrigan, C.R., Brecque, D.L., Kharaka, Y.K., Thordsen, J.J., Phelps, T.J., Yang, C., Romanak, K.D., Zhang, T., Holt, R.M., Lindler, J.S., Butsch, R.J., 2011. Monitoring a large volume CO2 injection: year two results from SECARB project at Denbury's Cranfield, Mississippi, USA. Energy Procedia 4, 3478–3485.

Hübert, J., 2012. From 2D to 3D models of electrical conductivity based upon magnetotelluric data, experiences from two case studies. Ph.D. thesis, Uppsala University, Sweden.

Jenkins, C., Chadwick, A., Hovorka, S.D., 2015. The state of the art in monitoring and verification - Ten years on. International Journal of Greenhouse Gas Control 40, 312-349.

Kiessling, D., Schmidt-Hattenberger, C., Schuett, H., Schilling, F., Krueger, K., Schoebel, B., Danckwardt, E., Kummerow, J., 2010. Geoelectrical methods for monitoring geological CO_2 storage: first results from cross-hole and surface-downhole measurements from the CO2SINK test site at Ketzin (Germany). International Journal of Greenhouse Gas Control 4, 816–826.

Koch, K., Wenninger, J., Uhlenbrook, S., and Bonell, M., 2009. Joint interpretation of hydrological and geophysical data: Electrical resistivity tomography results from a process hydrological research site in the Black Forest Mountains, Germany. Hydrol. Process. 23, 1501–1513.

Kordi, M., Hovorka, S., Milliken, K., Trevino, R., Lu, J., 2010. Diagenesis and reservoir heterogeneity in the lower Tuscaloosa Formation at Cranfield Field, Mississippi. Gulf Coast Association of Geological Societies Transactions 60, 809.

Kowalsky, M.B., Gasperikova, E., Finsterle, S., Watson, D., Baker, G., Hubbard, S.S., 2011. Coupled modeling of hydrogeochemical and electrical resistivity data for exploring the impact of recharge on subsurface contamination. Water Resources Research 47, W02509, doi:10.1029/2009WR008947.

LaBrecque, D.J., Ramirez, A.L., Daily, W.D., Binley, A.M., Schima, S.A., 1996. ERT monitoring of environmental remediation processes. Measurement Science and Technology 7, 375-383.

Lamert, H., Geistlinger, H., Werban, U., Schütze, C., Peter, A., Hornbruch, G., Schulz, A., Pohlert, M., Kalia, S., Beyer, M., Großmann, J., Dahmke, A., Dietrich, P., 2012. Feasibility of geoelectrical monitoring and multiphase modeling for process understanding of gaseous CO_2 injection into a shallow aquifer. Environ. Earth Sci. 67, 447–462.

Li, Y., Oldenburg, D.W., 1998. 3-D inversion of gravity data. Geophysics 63, 109–119.

Lu, J., Cook, P.J., Hosseini, S.A., Yang, C., Romanak, K.D., Zhang, T., Freifeld, B.M., Smyth, R.C., Zeng, H., Hovorka, S.D., 2012, Complex fluid flow revealed by monitoring CO2 injection in a fluvial formation. J. Geophys. Res., 117, B03208, doi:10.1029/2011JB008939.

Lu, J., Kordi, M., Hovorka, S.D., Meckel, T.A., Christopher, C.A., 2013. Reservoir characterization and complications for trapping mechanisms at Cranfield CO2 injection site. International Journal of Greenhouse Gas Control 18, 361–374.

Newman, G.A., Alumbaugh, D.L., 2000. Three-dimensional magnetotelluric inversion using non-linear conjugate gradients. Geophysical Journal International 140, 410-424.

Nimmer, R.E., Osiensky, J.L., Binley, A.M., Williams, B.C., 2008. Three-dimensional effects causing artifacts in two-dimensional, cross-borehole, electrical imaging, Journal of Hydrology 359, 59-70.

Papadopoulos, N.G., Tsourlos, P., Tsokas, G.N., Sarris A., 2007. Efficient ERT measuring and inversion strategies for 3D imaging of buried antiquities, Near Surface Geophysics 5, 349 - 361, DOI: 10.3997/1873-0604.2007017.

Ramirez, A., Newmark, R.L., Daily, W.D., 2003. Monitoring carbon dioxide floods using electrical resistance tomography (ERT): sensitivity studies. Journal of Environment Engineering Geophysics 8, 187–208.

Rücker, C., Günther, T., Spitzer, K., 2006. Three-dimensional modelling and inversion of dc resistivity data incorporating topography - I. Modelling. Geophysical Journal International 166, 495-505.

Schmidt-Hattenberger, C., Bergmann, P., Bösing, D., Labitzke, T., Möller, M., Schröder, S., Wagner, F., Schütt, H., 2013. Electrical resistivity tomography (ERT) for monitoring of CO_2 migration - from tool development to reservoir surveillance at the Ketzin pilot site. Energy Procedia 37, 4268 – 4275.

Spetzler, J., Xue, Z., Saito, H., Nishizawa, O., 2008. Case story: time-lapse seismic crosswell monitoring of CO_2 injected in an onshore sandstone aquifer. Geophys. J. Int. 172, 214–225.

Strazisar, B.R., Wells, A.W., Diehl, J.R., Hammack, R.W. , Veloski, G.A., 2009. Near-surface monitoring for the ZERT shallow CO_2 injection project. International Journal of Greenhouse Gas Control 3, 736–744.

Trautz, R.C., Pugh, J.D., Varadharajan, C., Zheng, L., Bianchi, M., Nico, P.S., Spycher, N.F., Newell, D.L., Esposito, R.A., Wu, Y., Dafflon, B., Hubbard, S.S., Birkholzer, J.T., 2013. Effect of dissolved CO_2 on a shallow groundwater system: a controlled release field experiment. Environ. Sci. Technol. 47, 298-305.

Wilt, M.J., Alumbaugh, D.L., Morrison, H.F., Becker, A., Lee, K.H., Deszcz-Pan, M., 1995. Crosswell electromagnetic tomography: System design considerations and field results. Geophysics 60, 871–885.

Wang, Z., Cates, M., Langan, R., 1998. Seismic monitoring of a CO_2 flood in a carbonate reservoir: a rock physics study. Geophysics 63, 1604–1617

Yang, X., Mats, L., 2006, Comparison of 2D and 3D Electrical Resistivity Imaging Methods, 19th EEGS Symposium on the Application of Geophysics to Engineering and Environmental Problems, DOI: 10.4133/1.2923695.

Yang, X., Lassen, R.N., Jensen, K.H., Looms, M.C., 2015. Monitoring CO_2 migration in a shallow sand aquifer using 3D crosshole electrical resistivity tomography. International Journal of Greenhouse Gas Control 42, 534-544.

Zhdanov, M., 2002. Geophysical inverse theory and regularization problems, Elsevier, Amsterdam.

Zhang, F., Juhlin, C., Cosma, C., Tryggvason, A., Pratt, R.G., 2012. Cross-well seismic waveform tomography for monitoring CO_2 injection: a case study from the Ketzin Site, Germany. Geophys. J. Int. 189, 629–646.

Zheng, L., Apps, J.A., Zhang, Y., Xu, T., Birkholzer, J.T., 2009. On mobilization of lead and arsenic in groundwater in response to CO_2 leakage from deep geological storage. Chem. Geol. 268, 281−297.

Figure Captions

Figure 1: Schematic view of the shallow injection site near the Victor J. Daniel Electric Generating Plant, Escatawpa (Mississippi). (a) Location of pumping, injection and monitoring wells. Also shown are well screened intervals. (b) ERT electrode layout within the screened intervals. Each screened zone contains a 4.55 m long electrode array, installed as a borehole cable hanging within the screened casing. Separations between all wells are shown in meters. The blue lines mark positions of model cross sections created from inverted data to be shown further below. The table lists all well coordinates.

Figure 2: 3-D view of the spatial gradient weighting function used for focusing of the inversion domain. The color denotes the weight assigned to each component of the gradient vector computed through the NLCG optimization scheme. Each gradient vector component represents one finite-difference grid cell parameter of the model search space.

Figure 3: First synthetic data inversion of the shallow injection experiment. Each set of three panels (a, b, c) shows the 2D sections Easting-Depth, Northing-Depth and Easting-Northing. (a) True electrical resistivity model. The target is represented by a conductive anomaly (10 Ωm) with ellipsoidal shape embedded in a 47.6 Ωm resistive half space. (b) Synthetic inversion result without using the gradient weighting technique. (c) Synthetic inversion result with application of the gradient weighting.

Figure 4: Sensitivity maps for the inversion domain of the shallow injection experiment data at Escatawpa. (a) horizontal cross section through z=49.75 m, (b) vertical cross section through y=299 m.

Figure 5a: 2-D Easting-versus-depth slices of 3-D time-lapse imaging results of the Escatawpa shallow injection experiment data. Each row of plots is a time in days after injection began, where each row contains 2-D *Easting-Depth* slices through three different Northing coordinates (marked by blue lines in Figure 1). The slice's Northing coordinates in the left, middle, and right plot columns are, respectively, N=292 m (southern slice, near MW-2), N=300 m (center slice, between MW-2 and MW-1), and N=307 m (northern slice, near MW-1). Projected into each subplot are the electrodes of wells MW-4 and MW-3. Shown are resistivity differences in % with respect to the pre-injection state.

Figure 5b: Northing-versus-depth 2-D slices of 3-D time-lapse imaging results of the Escatawpa shallow injection experiment data. Each row of plots is a day after injection began, where each row contains slices through three different Easting coordinates (marked by blue lines in Figure 1). The slice's Easting coordinates in the left, middle, and right plot columns are, respectively, E=514 m (eastern slice, near MW-3), E=507 m (center slice, between MW-4 and MW-3), and E=499 m (western slice, near MW-4). Projected into each subplot are the electrodes of wells MW-2 and MW-1. Shown are resistivity differences in % with respect to the pre-injection state.

Figure 6: Second synthetic inversion study of the shallow injection experiment. Synthetic data was created from the model obtained from inverting the Escatawpa data for day 131 (shown by the left column and by Figure 5 a and b, bottom panel). Two comparative inversions have the weighted gradients inactive (middle column) and active (right column).

Figure 7: Supercritical CO_2 injection site at Cranfield, 12 miles east of Natchez (MS) as presented in

Commer et al. (2014). (a) The aerial view of the site includes the F-1 injector and the two monitoring drillholes (F-2 and F-3). (b) The complete 3-D mesh used for hydrological inverse modeling is shown by the upper panel, with a close-up view in the lower panel. Symmetry considerations in the hydrological modeling limit the degrees of freedom to only one quarter of the simulation domain. Red crosses show measurement locations of gas mole-fraction data in wells F-2 and F-3. Blue dots indicate mesh elements over which electrical conductivity (EC) data are averaged into temporal changes, $\sigma(t)/\sigma(t=0)$, that serve as hydrological proxy data.

Figure 8: Sensitivity map for the Cranfield site. Sensitivities are represented as $\log_{10}(S_m^{norm})$, where S_m^{norm} are the individual cell sensitivities calculated using Equation 1 and normalized over the global maximum.

Figure 9: Changes in resistivity produced from the imaging tool BERT, where the left panels show 2-D inversion results and the right panels show 3-D inversion results. The isosurfaces in the 3-D panels indicate regions where the resistivity increase exceeds 20 %. The approximate boundaries of the reservoir storage zone are indicated by the two lines in the first panel.

Figure 10: Changes in resistivity produced from 3-D inversions using the imaging tools BERT (left panels) and EMGeo (right panels). The isosurfaces in the 3-D panels indicate regions where the resistivity increase exceeds 20 %.

Figure 11: Hydraulic permeability model integrated with the isosurfaces of resistivity changes over 5 % (grey) and 20 % (red). Resistivity changes are derived from the EMGeo imaging result for day 103 (also shown in the right column of Figure 10).

Tables

Source-dipole well	Receiver-dipole well	Number of source-receiver dipole pairs
MW-3	MW-4	182
MW-2	MW-1	182
MW-2	MW-3	182
MW-1	MW-3	182
MW-2	MW-4	182
MW-4	MW-1	160
Total:		1070

Table 1: Summary of the survey configuration for the inverted ERT data from the shallow injection experiment at the Victor J. Daniel Electric Generating Plant. The data contains all six transects between the four monitoring wells, with a total of 1070 source-receiver configurations. For example: The number of inverted data with source dipole electrodes in well MW-3 and receiver dipole electrodes in MW-4 is 182.

Figures

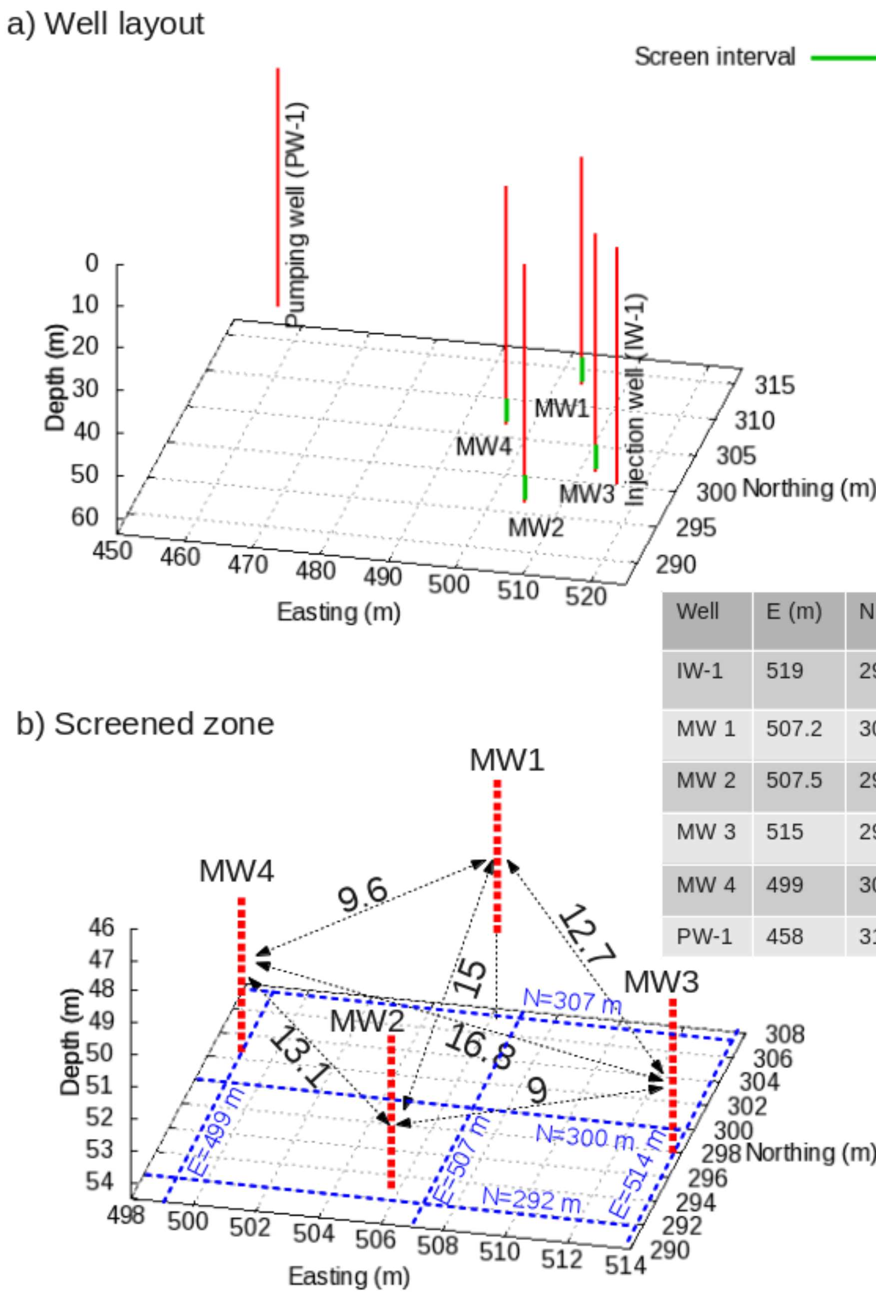

Well	E (m)	N (m)
IW-1	519	295.5
MW 1	507.2	307
MW 2	507.5	292
MW 3	515	297
MW 4	499	302
PW-1	458	315

Figure 1

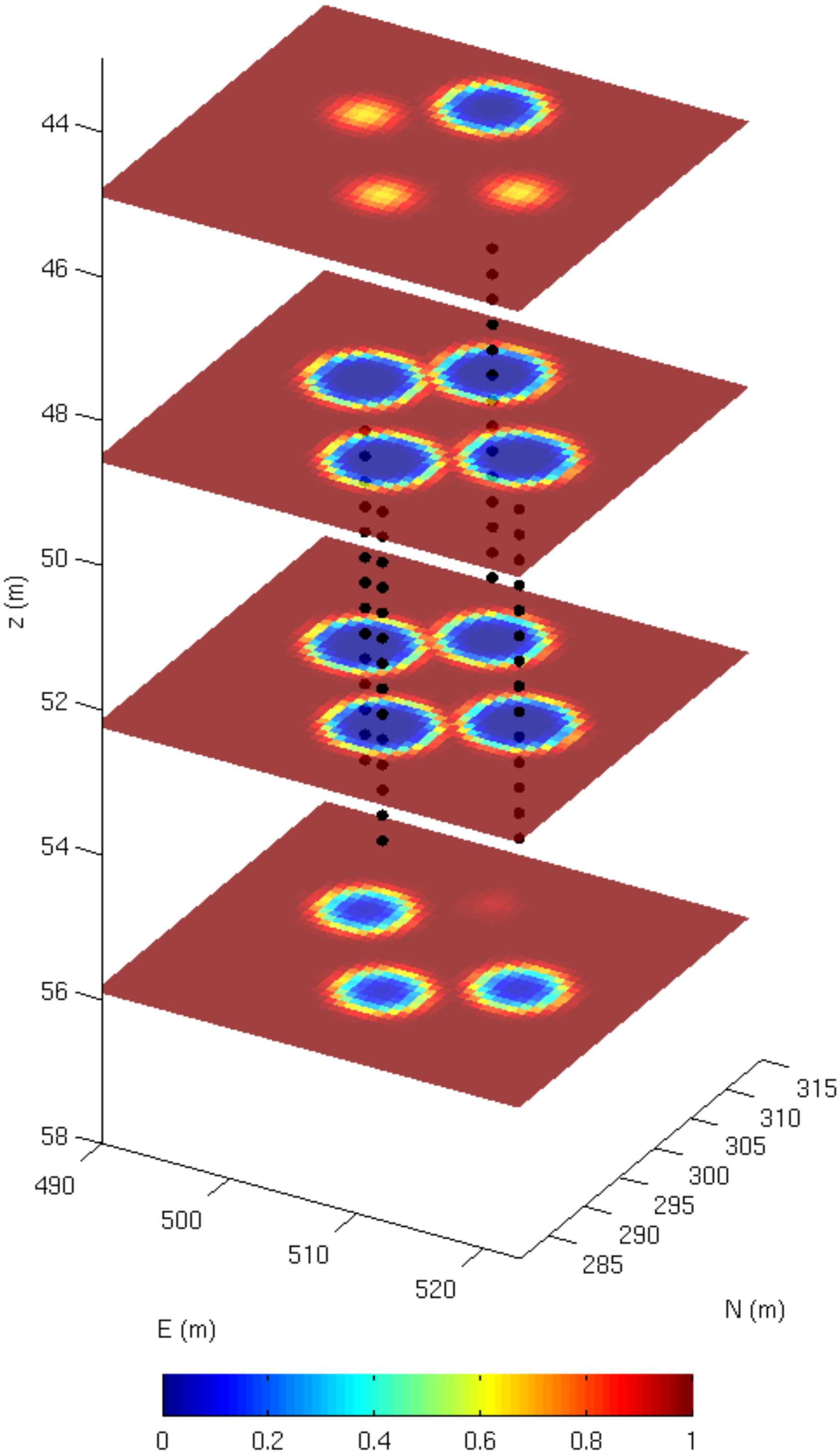

808
809 Figure 2

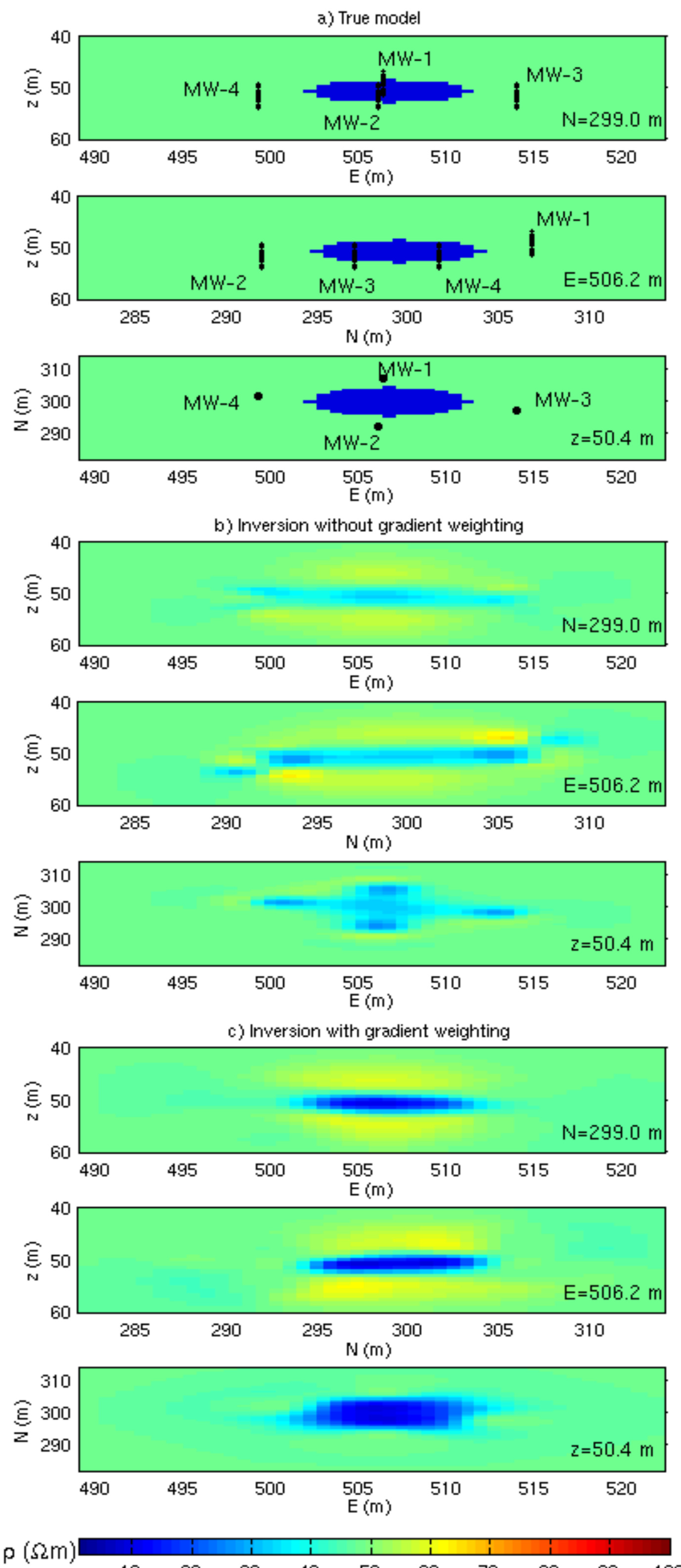
a) True model
MW-1
MW-2
MW-3
MW-4
N=299.0 m
E=506.2 m
z=50.4 m
z (m)
N (m)
E (m)
b) Inversion without gradient weighting
c) Inversion with gradient weighting
ρ (Ωm)

Figure 3

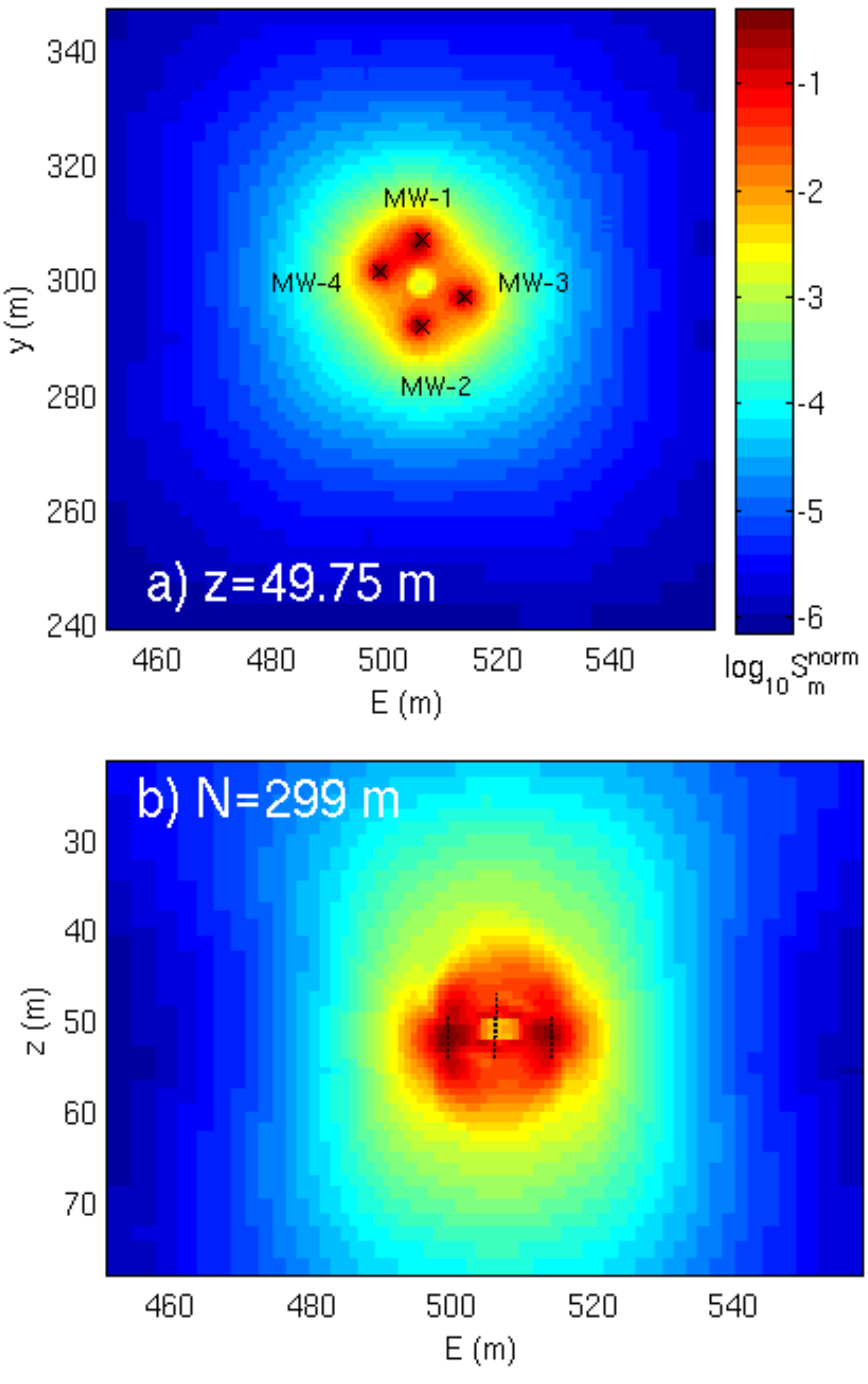

Figure 4

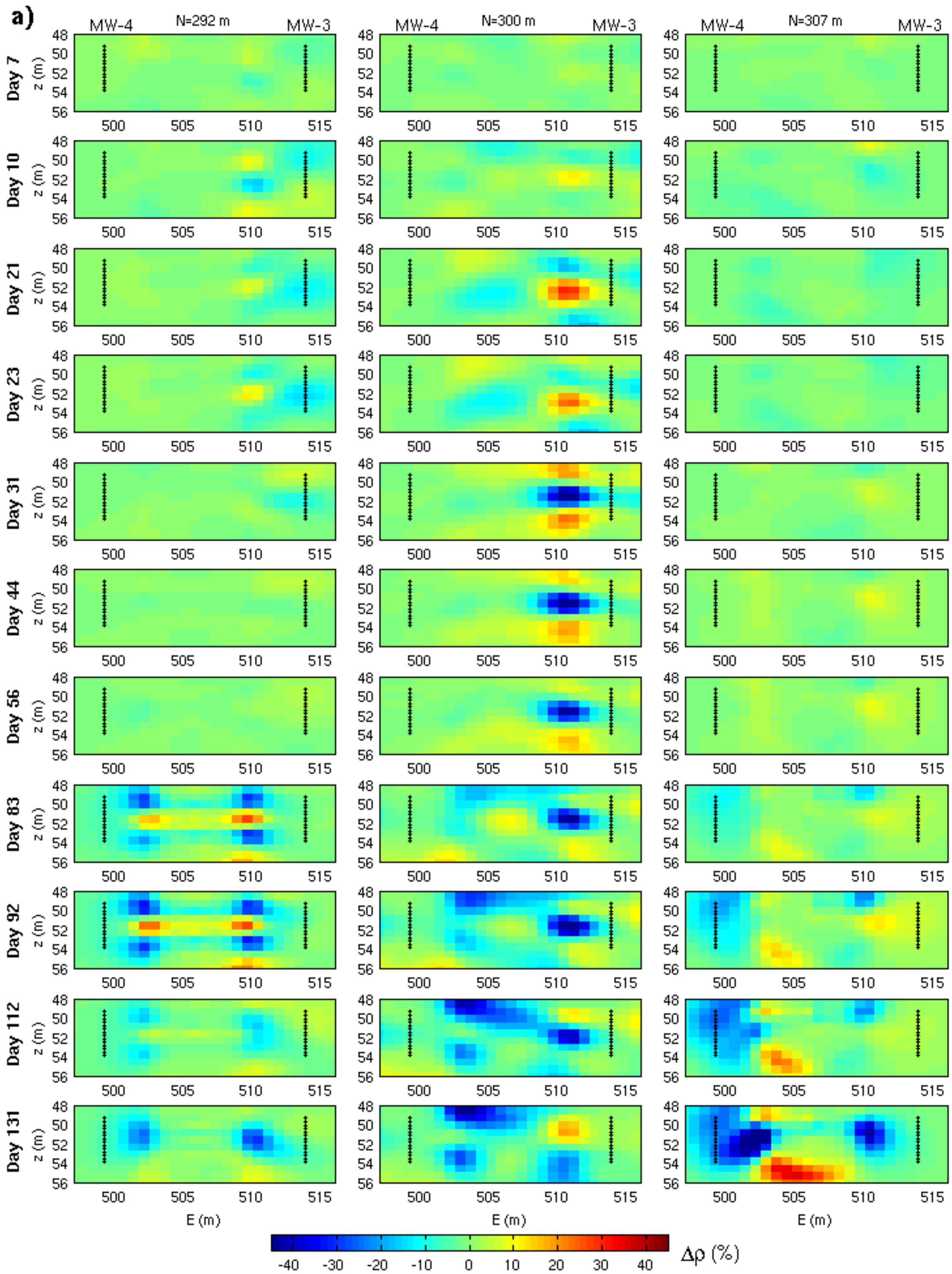
a)
MW-4
N=292 m
MW-3
MW-4
N=300 m
MW-3
MW-4
N=307 m
MW-3
Day 7
Day 10
Day 21
Day 23
Day 31
Day 44
Day 56
Day 83
Day 92
Day 112
Day 131
z (m)
48
50
52
54
56
500
505
510
515
E (m)
-40
-30
-20
-10
0
10
20
30
40
Δρ (%)

Figure 5a

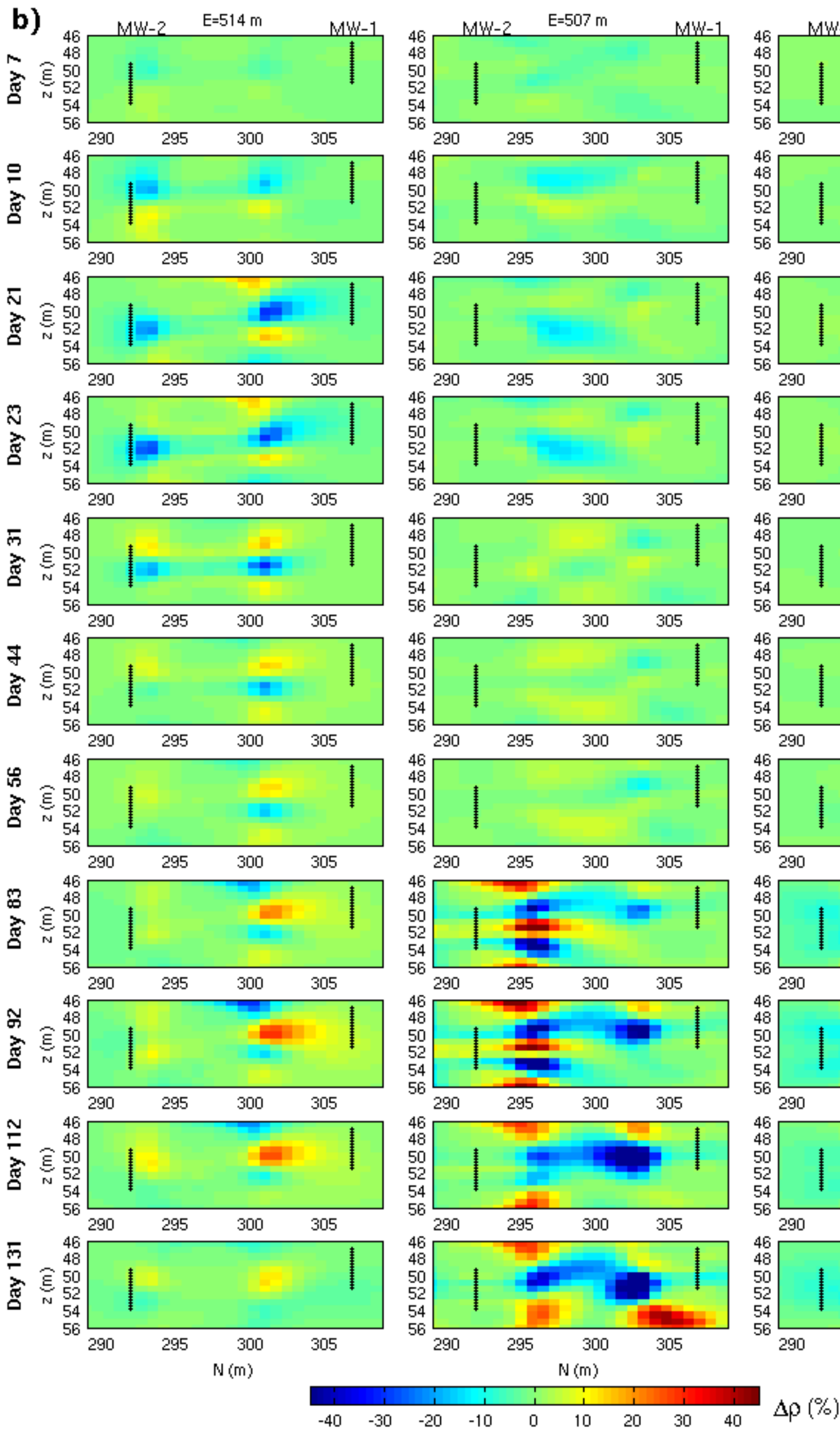
b)
MW-2
E=514 m
MW-1
E=507 m
E=499 m
Day 7
Day 10
Day 21
Day 23
Day 31
Day 44
Day 56
Day 83
Day 92
Day 112
Day 131
z (m)
46
48
50
52
54
56
290
295
300
305
N (m)
-40
-30
-20
-10
0
10
20
30
40
Δρ (%)

Figure 5b

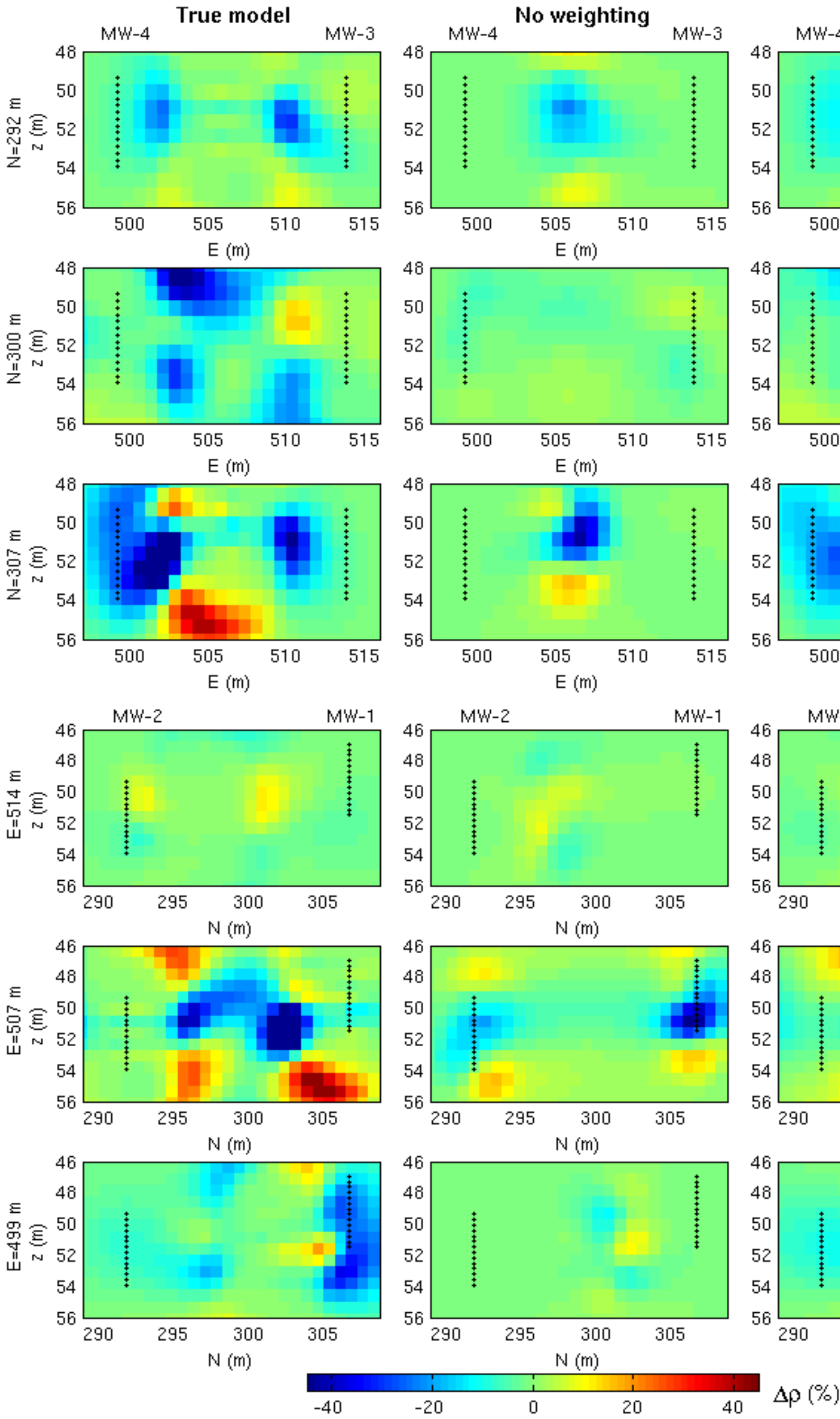

822
823 Figure 6
824

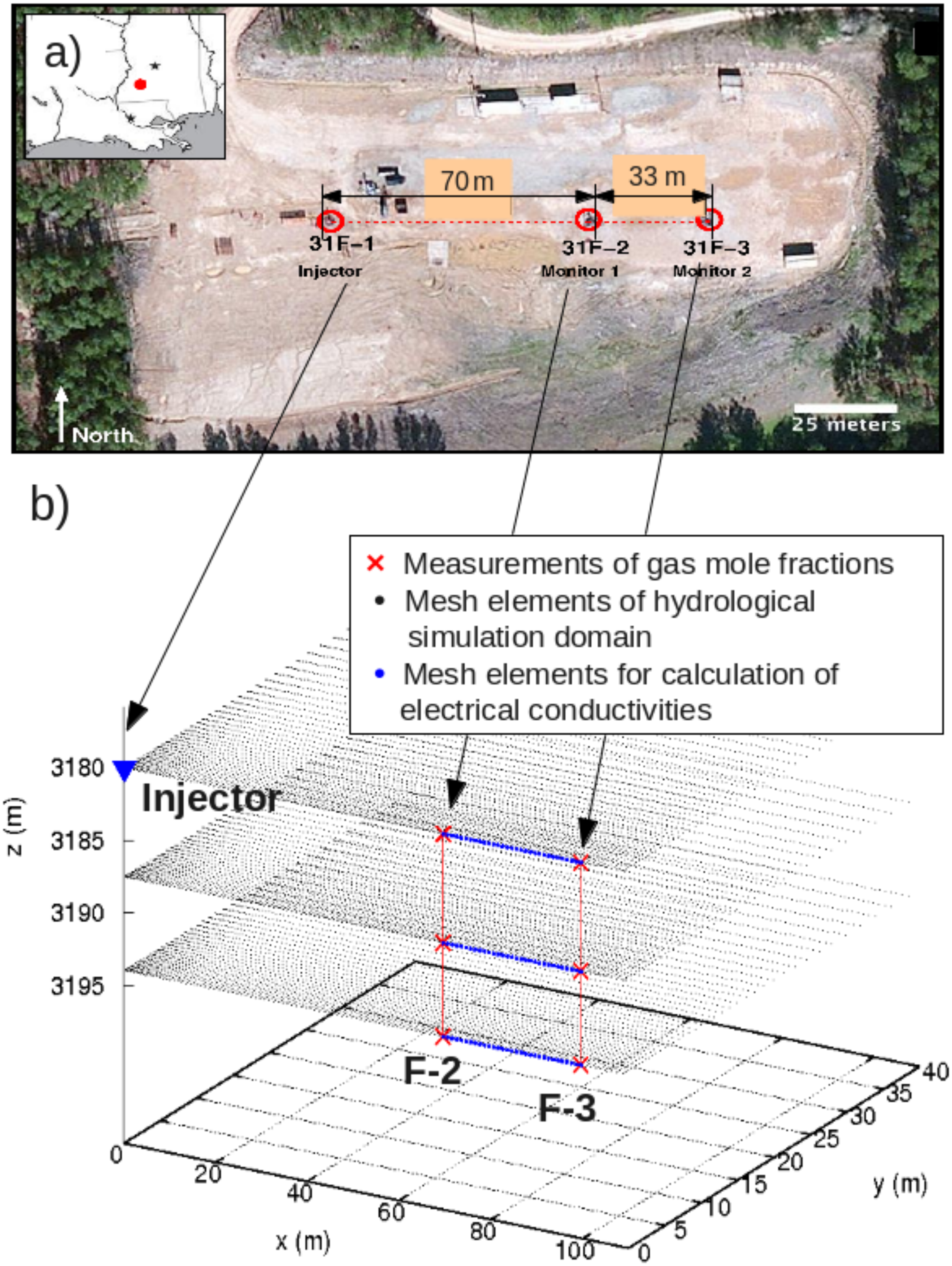
a)
70 m
33 m
31F−1
Injector
31F−2
Monitor 1
31F−3
Monitor 2
North
25 meters
b)
Measurements of gas mole fractions
Mesh elements of hydrological simulation domain
Mesh elements for calculation of electrical conductivities
Injector
F-2
F-3
z (m)
3180
3185
3190
3195
0
20
40
60
80
100
x (m)
0
5
10
15
20
25
30
35
40
y (m)

Figure 7

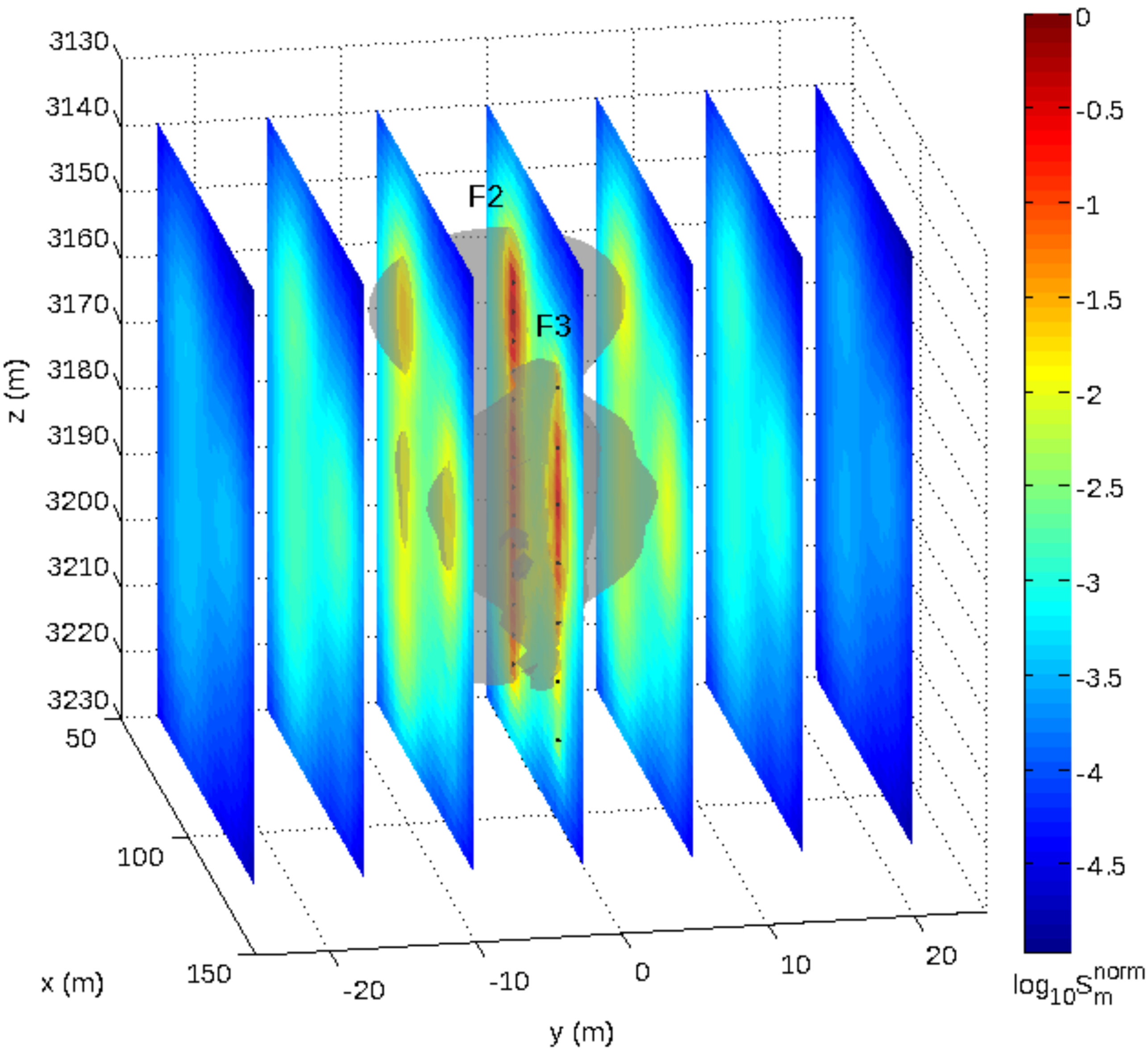
3130
3140
3150
3160
3170
3180
3190
3200
3210
3220
3230
z (m)
F2
F3
50
100
150
x (m)
-20
-10
0
10
20
y (m)
0
-0.5
-1
-1.5
-2
-2.5
-3
-3.5
-4
-4.5
$\log_{10}S_m^{norm}$

Figure 8

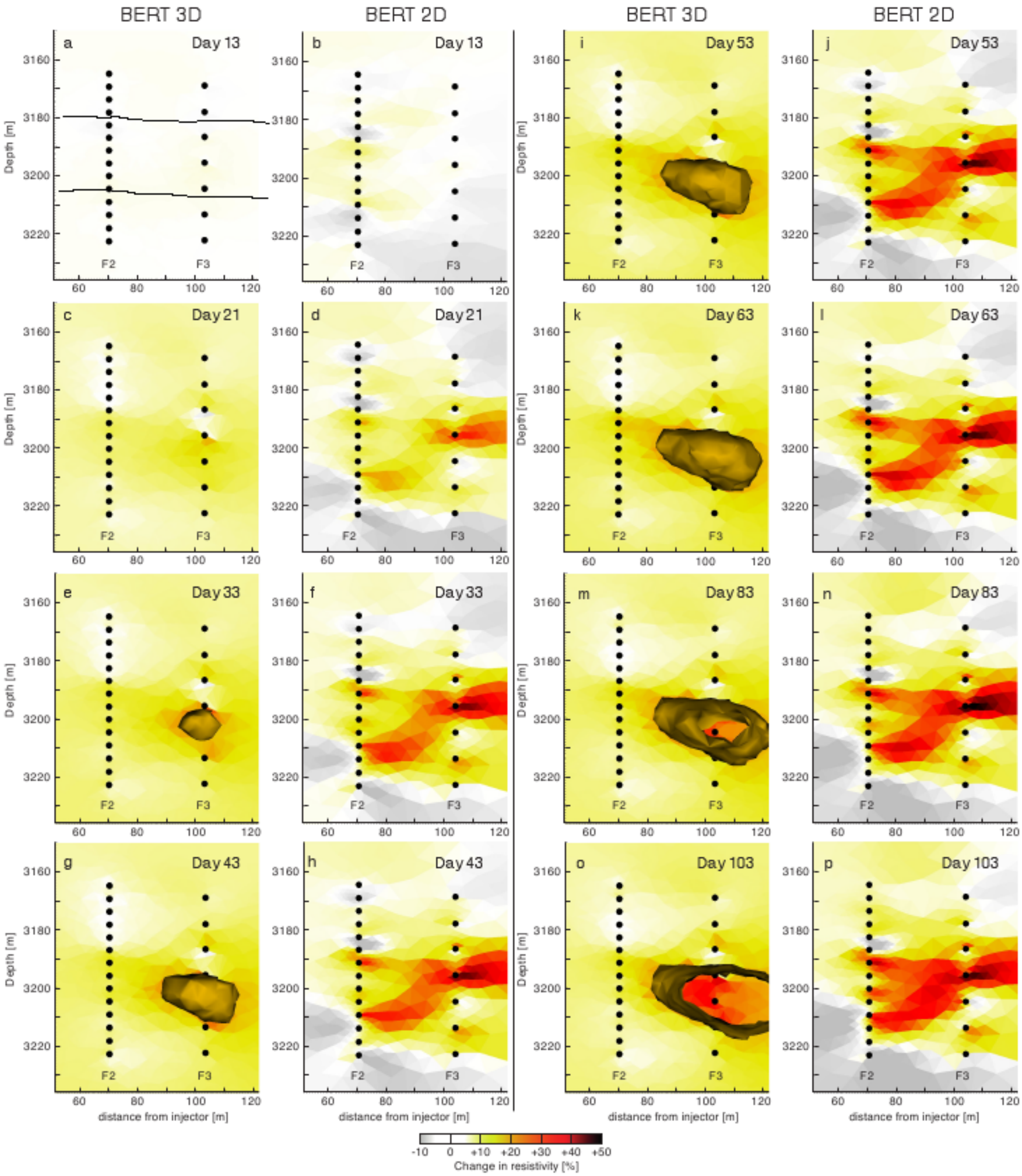

BERT 3D
BERT 2D
BERT 3D
BERT 2D
a
Day 13
b
Day 13
i
Day 53
j
Day 53
c
Day 21
d
Day 21
k
Day 63
l
Day 63
e
Day 33
f
Day 33
m
Day 83
n
Day 83
g
Day 43
h
Day 43
o
Day 103
p
Day 103
Depth [m]
F2
F3
distance from injector [m]
Change in resistivity [%]

Figure 9

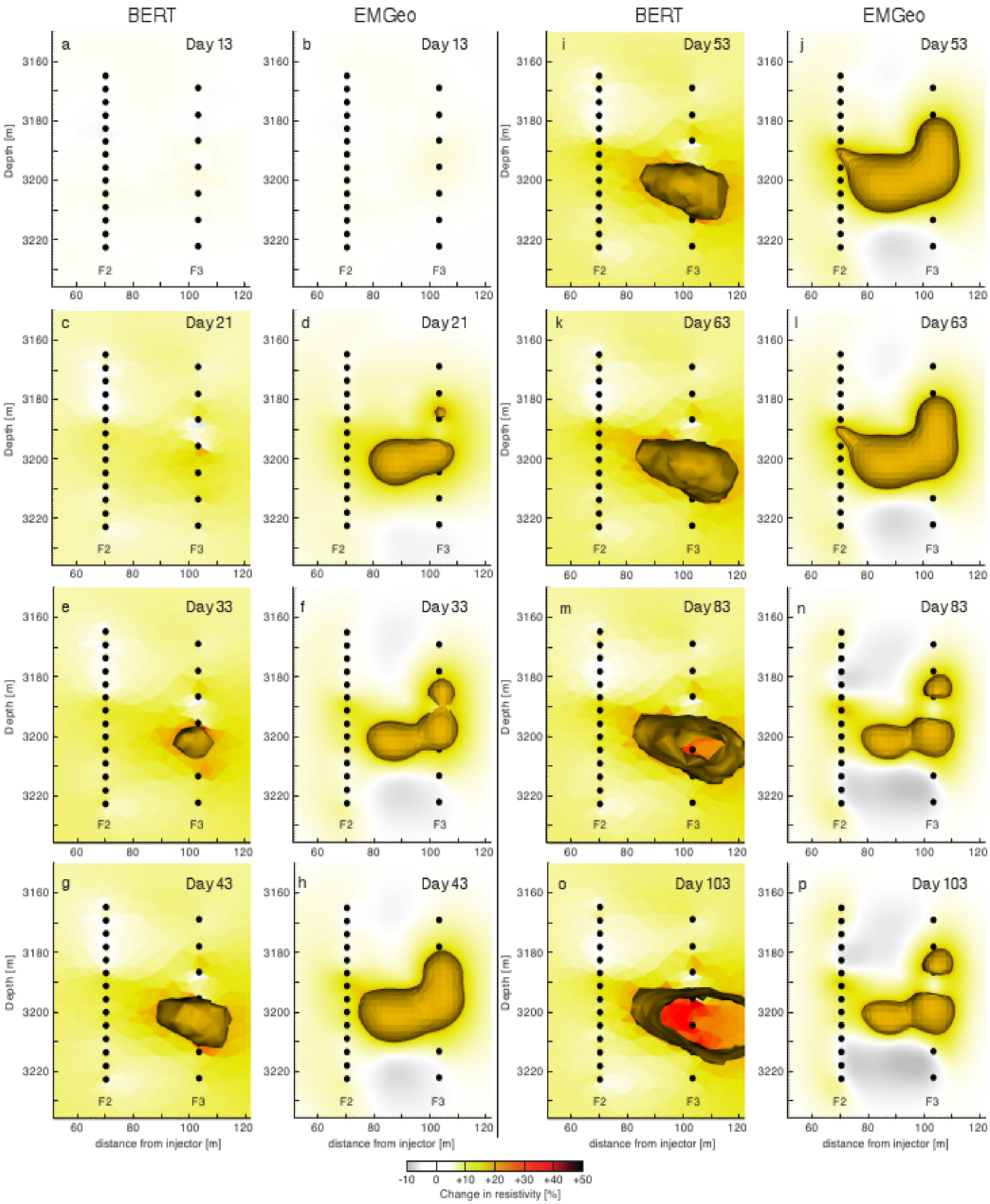
BERT
EMGeo
BERT
EMGeo
a Day 13
b Day 13
i Day 53
j Day 53
c Day 21
d Day 21
k Day 63
l Day 63
e Day 33
f Day 33
m Day 83
n Day 83
g Day 43
h Day 43
o Day 103
p Day 103
Depth [m]
3160
3180
3200
3220
F2
F3
60
80
100
120
distance from injector [m]
-10
0
+10
+20
+30
+40
+50
Change in resistivity [%]

Figure 10

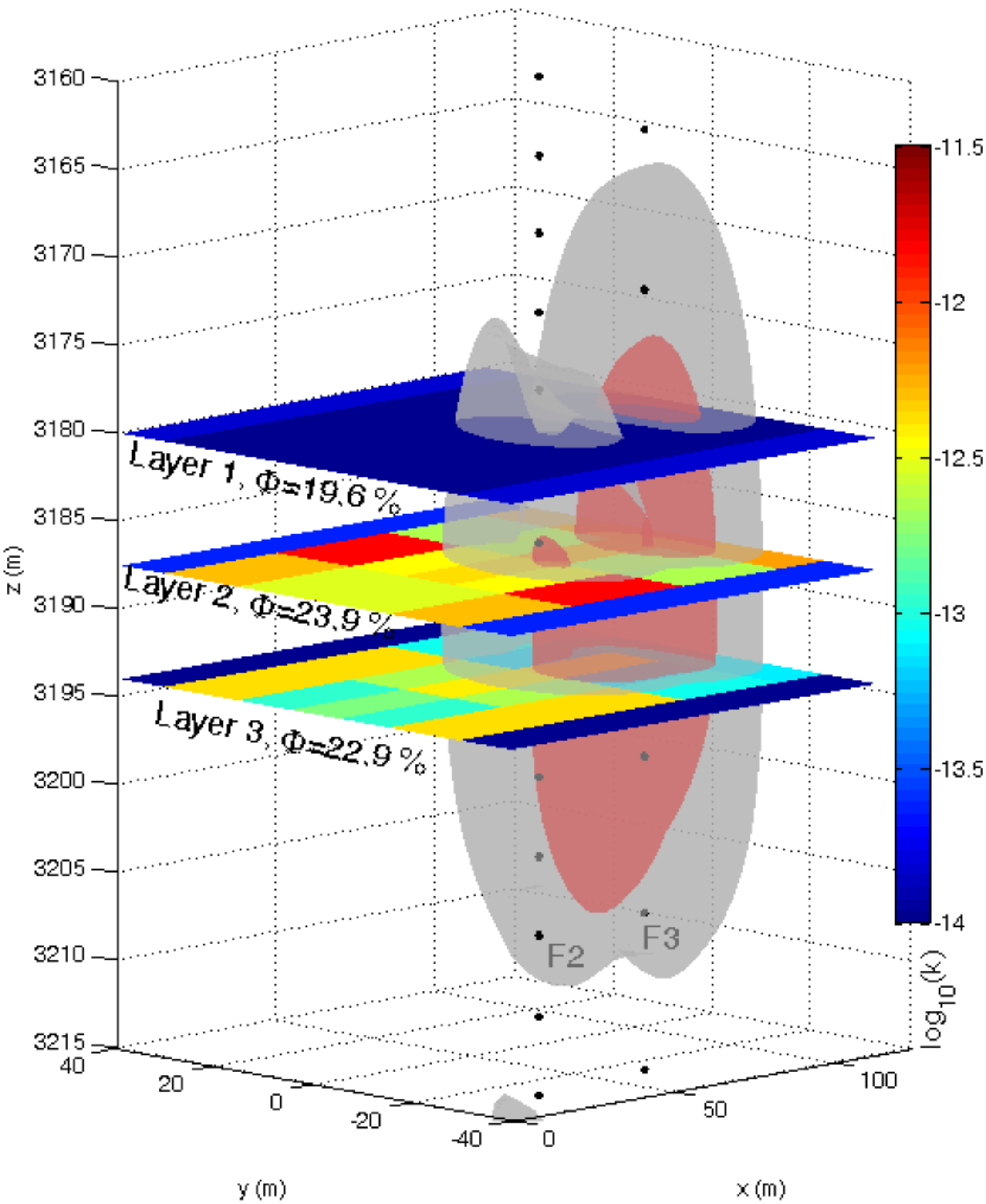
z (m)
3160
3165
3170
3175
3180
3185
3190
3195
3200
3205
3210
3215
Layer 1, Φ=19.6 %
Layer 2, Φ=23.9 %
Layer 3, Φ=22.9 %
F2
F3
y (m)
40
20
0
-20
-40
x (m)
0
50
100
-11.5
-12
-12.5
-13
-13.5
-14
log10(k)

Figure 11